





Space-Borne GNSS-R Signal Over a Complex Topography: Modeling and Validation

Laura Dente , Leila Guerriero , *Member, IEEE*, Davide Comite , *Member, IEEE*,
and Nazzareno Pierdicca , *Senior Member, IEEE*

Abstract—A significant quantity of space-borne Global Navigation Satellite Systems-Reflectometry (GNSS-R) data over land was made available in the last decade, leading to an increasing interest in the assessment of the potentialities of this new remote sensing technique for land monitoring. In this frame, an electromagnetic simulator, such as the Soil And VEgetation Reflection Simulator (SAVERS), has the key role to support the understanding of the physical mechanism involved in the bistatic scattering and to identify the surface features mainly contributing to the observed signal. Originally developed for ground and airborne GNSS-R observations over homogeneous areas, in this study, SAVERS was upgraded to account for space-borne systems. The new version of SAVERS takes into account the inhomogeneity characterizing the large area observed from space altitudes, due to a variable surface elevation and land cover. Coherent and incoherent scattering and polarization rotation are computed taking into account the local slope and elevation of the surface. The simulator was validated against TechDemoSat-1 observations over a bare surface with a complex topography and over a forested surface with a gentle topography. The validation results show the capability of SAVERS to correctly estimate the effect of the topography, enhancing the understanding of the observations. Moreover, it was found that the sensitivity to soil moisture is independent of the topography (about 1.5 dB for a 10% variation of soil moisture). Whereas a saturation of the GNSS-R reflectivity over a variable topography is reached for lower values of biomass, earlier than in the flat case.

Index Terms—Global Navigation Satellite Systems (GNSS) reflectometry, land applications, scattering model, simulator, surface topography, TechDemoSat-1 (TDS-1).

I. INTRODUCTION

GLOBAL Navigation Satellite Systems-Reflectometry (GNSS-R) is a relatively new remote sensing technique that takes advantage of the signal transmitted by sensors already in place, such as the Global Positioning System (GPS) to characterize the scattering features of the Earth surface mainly along the specular direction. It makes use of a low-cost passive receiver

to observe the reflections from ocean, bare soils, and vegetated surfaces [1], [2]. The received signal carries information on the physical characteristics of the illuminated surfaces and depends on the properties of the receiving system. The technique was originally developed for ocean applications; however, several experiments carried out by means of ground- and air-borne receivers showed the potentialities for land applications as well [3]–[6]. These studies demonstrated the sensitivity of GNSS-R observations to land parameters, such as soil moisture, vegetation biomass, and inland water, and foresaw the potential contributions of space-borne GNSS-R observations to land surface monitoring. After the launch of TechDemoSat-1 (TDS-1) satellite in 2014 and of the Cyclone Global Navigation Satellite System (CYGNSS) constellation in 2016, both having aboard a GNSS-R payload, a large amount of space-borne GNSS-R observations have been made available, therefore boosting the investigations of the possibility of retrieving land surface parameters by means of this technique [7], [8].

In this frame, an electromagnetic model capable to simulate the GNSS-R observations over land can be a valuable tool to improve the understanding of the physical mechanisms involved in the bistatic scattering, as well as to single out the contribution of all scatterers to the coherent and incoherent components of the signal. Models also allow the investigation of the effects of the involved surface parameters on the observations from space and the evaluation of the potentialities and limitations of the GNSS-R technique in the retrieval of land surface parameters.

The theoretical characterization of waveforms or delay-Doppler maps (DDM) was originally accomplished by Zavorotny and Voronovich [9], and more recently further elaborated in [10]. This approach has been mainly used for ocean applications and included in several simulation tools. For example, Park *et al.* [11] proposed an end-to-end simulator taking into account ionospheric and tropospheric effects, as well as system noise. This simulator has been recently updated to include the land reflection coefficient [12]. An open-source software library, WAVPY, was created by Fabra *et al.* [13] consisting of object-oriented classes, each of them simulating one of the aspects involved in GNSS-R acquisitions. A forest model was proposed by Wu and Jin [14] on the basis of Bi-Mimics model (Bi-Michigan Microwave Canopy Scattering) [15]. Eroglu *et al.* [16] developed a model for corn based on the coherent SCoBi-Veg model (Signals of opportunity COherent Bistatic scattering for VEGetated terrain) [17]. Both models were used to analyze the GNSS-R sensitivity to various land parameters,

Manuscript received December 23, 2019; revised February 4, 2020; accepted February 5, 2020. Date of publication March 16, 2020; date of current version April 13, 2020. This work was supported by the European Space Agency ESA/ESTEC under Contract No. 4000120299/17/NL/AF/hh. (Corresponding author: Laura Dente.)

Laura Dente and Leila Guerriero are with the Department of Civil Engineering and Computer Science, Tor Vergata University of Rome, Rome 00133, Italy (e-mail: laura.dente@uniroma2.it; leila.guerriero@uniroma2.it).

Davide Comite and Nazzareno Pierdicca are with the Department of Information Engineering, Electronics and Telecommunications, “Sapienza” University, Rome 00184, Italy (e-mail: davide.comite@uniroma1.it; nazzareno.pierdicca@uniroma1.it).

Digital Object Identifier 10.1109/JSTARS.2020.2975187

however, neither of them included the system response function or were validated against experimental data.

Gu *et al.* [18] and Zhu *et al.* [19] faced the topography issue in GNSS-R land observations applying the Kirchhoff approximation to rough patches. Intermediate results between a perfect coherent and a perfect incoherent approach were obtained.

The Soil And VEgetation Reflection Simulator (SAVERS) [20] is able to model the reflected GNSS-R signal and the DDM through the integral bistatic radar equation, following the approach by Zavorotny and Voronovich in [9], weighting the contributions of all scatterers on the surface by the Woodward ambiguity function (WAF). It accounts for the coherent component of the signal related to the reflection of the mean soil surface, as well as the incoherent component due to vegetation volume and rough soil scattering. The performances of the simulator were tested using the data collected in the Land MONitoring with Navigation signals (LEiMON) campaign by a ground-based sensor [5] and in the GNSS Reflectometry Analysis for biomaSS (GRASS) campaign by airborne sensors [6]. Overall, it was demonstrated that SAVERS is a valuable tool for an accurate interpretation of GNSS-R measurements over bare, agricultural, and forested areas.

However, in the case of a space-borne GNSS-R system, the area observed by the receiver is much larger than for low altitude sensors, and several aspects become relevant, such as the low magnitude reached by the reflected signal, the effect of the topography, as well as of the land cover inhomogeneity. Chew *et al.* [7] showed a decrease of the TDS-1 reflected power for increasing large-scale surface roughness, and Carreno-Luengo *et al.* [21] studied the effects of several topographic parameters on the waveform. Therefore, in this study, SAVERS was upgraded to consider a space-borne receiver and all related modeling issues.

The version of SAVERS here presented can process a digital elevation model (DEM) given as input to take into account the elevation, the slope, and the aspect angle of each elemental area of the simulation grid. Land cover inhomogeneities in the simulation area can be considered by the model as well. In this way, the local incidence and scattering direction are correctly computed for each elemental area, and the corresponding contribution to the total received signal is properly simulated, weighted, and integrated by the radar equation for each delay Doppler cell. In order to evaluate the performance of the current version of SAVERS, the simulations were run in the same observation geometry of TDS-1 and were compared with calibrated data. The validation was carried out over a bare area with a complex topography, such as that of Tibesti volcanic region in Chad and over an open forest located in southern Congo.

Moreover, the simulator was used to investigate the effect of the topography on the sensitivity of the space-borne GNSS-R signal to soil moisture and forest biomass. For this scope, soil moisture and biomass were varied keeping fixed the other input parameters and the corresponding variations of the simulated reflectivity was evaluated. The case of a flat terrain was compared to the case of a mountainous area.

Section II reviews the main characteristics of SAVERS and details the new features. Section III presents the results of the validation, and the results of the sensitivity analysis are reported

in Section IV. Finally, the main conclusions are drawn in Section V.

II. SAVERS

A. SAVERS General Structure

SAVERS was originally developed in the frame of two ESA projects, namely, LEiMON [5] and GRASS [6]. The general approach of the simulator follows the studies by Zavorotny and Voronovich [9] where a model of the bistatically reflected GPS signal over the ocean was theoretically formulated. The approach was adapted to the case of land and presented in detail in [20]. The formula at the core of SAVERS, which evaluates the cross-correlation between the received signal with a replica of the transmitted pseudorandom noise (PRN) code, is given as the following:

$$|Y_{rt}(\tau, f)|^2 = \frac{\lambda^2}{(4\pi)^3} P_T T_i^2 \iint \frac{G_T(\vartheta_i, \varphi_i) G_R(\vartheta_s, \varphi_s)}{R_R^2 R_T^2} \times \sigma_{rt}^0(\vartheta_i, \varphi_i; \vartheta_s, \varphi_s; \Theta) \Lambda^2(\delta\tau) S^2(\delta f) dA. \quad (1)$$

$Y_{rt}(\tau, f)$ is the output of the signal correlator as a function of the time delay τ and of the Doppler frequency f , i.e., the so-called DDM. λ , P_T , and G_T are the transmitted signal wavelength, the power, and the antenna gain of the transmitter, respectively. G_R is the antenna gain of the receiver; R_R is the distance from the receiver to the element dA of the integration area A on the Earth surface, and R_T is the distance from the transmitter to dA . σ_{rt}^0 is the dimensionless bistatic scattering coefficient of dA , where the subscripts r and t indicate the polarization of the received and transmitted signals, respectively. The scattering coefficient is a function of the incidence (ϑ_i, φ_i) and the scattering (ϑ_s, φ_s) angles at each surface element, as well as of the vector Θ that includes the geometric and dielectric properties of each element. Λ^2 is the GPS correlation (triangle) function that represents the impulse response of the system in the time domain for the GPS C/A code. S is the *sinc* function that represents the impulse response of the system in the frequency domain and depends on the coherent integration time T_i used in the signal processing. The longer is the integration time, the sharper is the filter in the frequency domain. $\delta\tau$ and δf are, respectively, the difference between the sampled time delay τ and a reference delay, and between the sampled frequency f and a reference Doppler frequency. The simulation area A is set large enough to take into account the significant contributions to the received signal. The area mainly contributing to the coherent part of the bistatic scattering coefficient for a plane surface can be approximated by the first Fresnel zone [22], [23], but the area contributing to the incoherent component can expand either to the entire antenna footprint, or to the delay-Doppler discrimination cell, whichever is the smaller. As well known, the space-borne GNSS-R system is a pulse-limited system, which means that the area mainly contributing to the signal reaching the receiver first in time is defined by the intersection of the first iso-range zone and the first Doppler zone. Receiver altitude, incidence angle, code chip length, and coherent integration time determine the size of the

two zones. As example, this area is approximately $40 \text{ km} \times 40 \text{ km}$ large in the case of TDS-1 for a 5° incidence angle. However, the received DDM includes contributions, although small, from the complete footprint of the receiver antenna that is approximately $600 \text{ km} \times 600 \text{ km}$ in the case of TDS-1 for a 5° incidence angle. The contributions coming from the border of the footprint, i.e., for large Doppler shifts and delays, are negligible and they do not determine the power and DDM shape around the peak. Therefore, the simulation area can be smaller than the antenna footprint, but should be larger than the first iso-range. SAVERS sets the width of the simulation area equal to two times the major semiaxis a of the maximum iso-range line to be simulated (given as input)

$$a = \frac{\sqrt{2\tau c H \cos \vartheta_i}}{\cos^2 \vartheta_i} \quad (2)$$

where τ is the maximum delay shift to be considered, c is the light speed, H is the receiver height with respect to the surface, and ϑ_i is the incidence angle.

It should be mentioned that Ferrazzoli *et al.* [24] demonstrated that the coherent scattering in the specular direction is important and can even overpass the incoherent scattering when the observed surface is characterized by small scale roughness with respect to the wavelength, like in the case of bare soil or vegetated fields. This is different from the ocean surface, and for this reason, SAVERS simulates both components.

SAVERS consists of three main modules: the GNSS-R geometry simulator, the bistatic scattering coefficient simulator (composed of two submodules for the case of bare and vegetated surfaces, respectively), and the DDM simulator. In the first module, SAVERS computes the geometric parameters characterizing the GNSS-R bistatic scenario [i.e., estimation of the position of the specular point (SP) on the mean Earth surface, typically the Earth ellipsoid, knowing position and velocity of transmitter and receiver; definition of the simulation reference system and of the simulation grid; computation of the incidence and scattering angles for each facet of the grid; computation of the ranges from the receiver and the transmitter to the facet and of the Doppler shift]. The second module calculates both coherent and incoherent bistatic scattering coefficients for each surface element, given the geophysical properties of the surface. The advanced integral equation model (AIEM) [25] is applied to compute the incoherent bistatic scattering of the soil. The coherent part is simulated upgrading the approach proposed in [26], as detailed in [22]. The bistatic scattering of the vegetation is computed through the Tor Vergata model [27], based on the solution of the radiative transfer equation for a medium made of randomly distributed scatterers representing the different vegetation elements. The last module calculates the integral in (1), delivering the DDM as well as its peak value.

The main steps of SAVERS formulation will be briefly described in this section with a focus on the upgrades introduced to simulate a space-borne GNSS-R receiver. The receiver position, i.e., latitude, longitude, and height above the ellipsoid, as well as the platform velocity, are SAVERS inputs. The transmitter position can be computed by means of an orbit propagator, using the satellite ephemerides from the GPS Yuma files, provided

that the satellite is in view of the receiver at the time of interest. Alternatively, if the position and velocity of the transmitter are provided with the GNSS-R data, they can be given directly as input to the simulator.

The original version of SAVERS assumes a flat Earth mean surface. First, the point on the Earth surface (approximated by an ellipsoid) that minimizes the transmitter-point-receiver path is searched. At this point, named flat surface SP, the incidence angle ϑ_i , and the scattering angle ϑ_s with respect to the normal to the surface are equal. Equation (1) is solved in the SAVERS global reference system (SGR) consisting of a rotated East-North-Up system. The SGR system is centered in the SP, the z -axis coincides with the geodetic vertical, the xy plane is tangent to the Earth's surface in the SP and it is rotated of an angle γ with respect to the East-North plane. This rotation should be such that the xz plane contains both transmitter and receiver, with the transmitter having a negative x coordinate and the receiver a positive one. The x and y coordinates are sampled to form a regular grid whose size and resolution are simulator inputs. All the quantities in the integral in (1), such as R_T , R_R , ϑ_s , and φ_s , are computed in the SGR frame and for each surface element $dA = dx dy$. The distance from the transmitter to the element and the incidence direction (namely, ϑ_i and φ_i) are assumed equal for all surface elements, due to the high orbit of the transmitter. Moreover, the azimuthal angle of the incidence direction (namely φ_i) is zero because of the chosen SGR frame conditions. The down-looking antenna gain pattern, together with its beamwidth, should be given as input, selecting either a generic cosinusoidal pattern, such as $G_R(\vartheta) = G_0 (\cos \vartheta)^n$, which is independent of the azimuth angle, or the real antenna gain of the receiver, if known.

It is worth mentioning that the $WAF = \Lambda^2(\delta\tau)S^2(\delta f)$ in (1) is expressed as a function of delay and Doppler shifts. Therefore, another grid with lines $k = 1, 2, \dots, K$, representing the frequency variable, and columns $l = 1, 2, \dots, L$, representing the time delay, is introduced. A transformation that maps the i, j indices (corresponding to equispaced samples of the x, y coordinates) into the l, k indices (corresponding to equispaced samples in the delay-Doppler plane) is carried out. Finally, the integral in (1) can be performed applying a conventional technique.

B. Geometric Module and Polarization Over Complex Topography

The main upgrades of SAVERS, developed in this work, concerned the capability of the simulator to take into account the inhomogeneities in the simulation area, due to variable terrain topography and land cover. This implied updates in various parts of the simulator. A DEM and a land cover map are required as input to the new version of SAVERS and properly processed for each surface element dA . This work focuses on the topography issue and the use of the DEM, only.

First, the DEM is used to refine the localization of the nominal SP. The mean DEM elevation around the flat surface SP (as described in the last section) is estimated. Then, the ellipsoid approximating the Earth is placed at a height corresponding to the mean DEM elevation and the point minimizing the

transmitter-point-receiver path is now identified on the larger ellipsoid. This is named nominal SP as it complies with the minimum path condition, however, the specular condition might not be met at this point due to the topography. Indeed, the presence of a local surface slope and aspect at the nominal SP might lead to an inequality between local incidence and scattering angle, therefore this point might not contribute to the reflected signal. The nominal SP is important since the origin of the SGR system is set in the projection of this refined SP on the ellipsoid. This is also the center of the simulation grid, as explained in the previous section.

The DEM is then interpolated on the simulation grid in the SGR system so that for each grid element (namely for each facet) the elevation is known. Afterward, the slope β and aspect α of each facet are calculated from the DEM elevations $h(x, y)$ through

$$\alpha = \text{atan} \left(\frac{dh}{dy} / \frac{dh}{dx} \right) \quad (3)$$

$$\beta = \text{atan} \left(\sqrt{\left(\frac{dh}{dx} \right)^2 + \left(\frac{dh}{dy} \right)^2} \right). \quad (4)$$

The slope angle is defined clockwise from the xy plane of the SGR system and ranges from 0° to 90° , and the aspect angle is defined clockwise from the SGR y axis and ranges from 0° to 360° .

The incidence and scattering angles at each facet are affected by the local slope and aspect. In order to facilitate the computation of the local incidence and scattering angle and the corresponding bistatic scattering coefficient, a local reference system is defined for each facet, called facet local reference $x'y'z'$ (FLR). The z' axes of the FLR system is orthogonal to the facet, while the $x'y'$ plane is tangential to the local facet surface. Each single $x'y'z'$ frame can be obtained through two rotations of the SGR system. The first is given by α around the z axis (with $0 \leq \alpha \leq 360^\circ$), which corresponds to the aspect, and the second by the angle β around the new y axis ($0 \leq \beta \leq 90^\circ$), which corresponds to the slope (see Fig. 1). The shift of the reference system origin in the center of each facet is disregarded in the definition of the FLR system since only a transformation of angles and vector rotations are involved in the computations at this step of the simulator.

The two rotations are described by the matrix U as follows:

$$U = \begin{bmatrix} \cos \alpha \cos \beta & \sin \alpha \cos \beta & -\sin \beta \\ -\sin \alpha & \cos \alpha & 0 \\ \cos \alpha \sin \beta & \sin \beta \sin \alpha & \cos \beta \end{bmatrix}. \quad (5)$$

The angles ϑ_i , ϑ_s , and φ_s in the SGR system define the incidence unit vector $\hat{l} = (\sin \vartheta_i, 0, \cos \vartheta_i)$, equal for all elemental areas, and the scattering unit vector $\hat{s} = (\sin \vartheta_s \cos \varphi_s, \sin \vartheta_s \sin \varphi_s, \cos \vartheta_s)$. The corresponding unit vector of the FLR frame can be obtained through the rotation: $\hat{l}' = U\hat{l}$ and $\hat{s}' = U\hat{s}$. Therefore, the local incidence angle (ϑ_{il} and φ_{il}) can be obtained by means of the following formula: $\cos \vartheta_{il} = z' \cdot \hat{l}'$, $\cos \varphi_{il} = x' \cdot \hat{l}' / \sin \vartheta_{il}$. Analogous formulas for \hat{s}' are used to compute the local scattering angles (ϑ_{sl} and φ_{sl}).

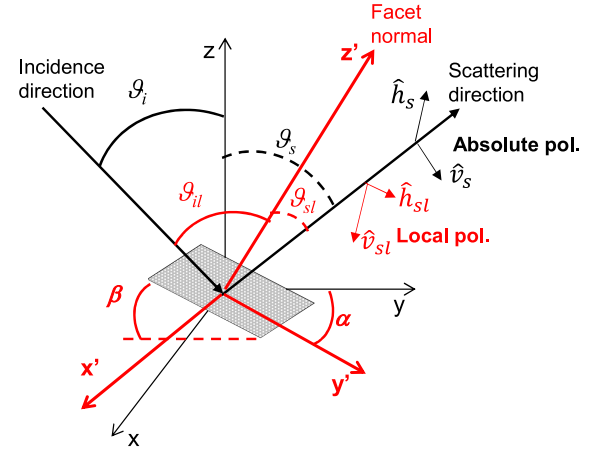


Fig. 1. SGR (xyz) system and FLR ($x'y'z'$) system; rotation angles α and β between the SGR system and the FLR system; incidence and scattering angles in the SGR system (ϑ_i and ϑ_s) and in the FLR system (ϑ_{il} and ϑ_{sl}); polarization vectors in the SLR (\hat{v} and \hat{h}) and in the FLR systems (\hat{v}_l and \hat{h}_l).

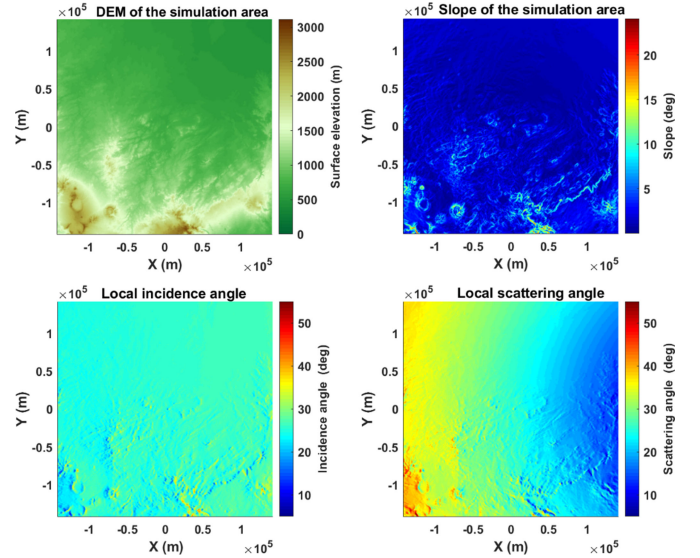


Fig. 2. Example of slope (top-right), local incidence (bottom left), and local scattering (bottom right) angle map computed by SAVERS for a mountainous area with DEM showed at top-left. All maps are in the SGR system.

Fig. 2 shows an example of the simulator processing results over an area characterized by a complex topography, located in Chad. The upper-left figure shows the DEM interpolated over the simulation grid (the elevations are referred to the ellipsoid). In the upper-right part of the figure, the slope of the area obtained from the DEM is shown. At the bottom of the figure, the map of the local incidence (left) and scattering (right) angles are reported. All maps are reported in the SGR system, meaning that the SP has (0, 0) coordinates, the projection of the transmitter is located along the negative x axis and the one of the receiver along the positive x axis. In this example, the transmitter and receiver coordinates of a real TDS-1 acquisition were used, where the GPS signal reached the area at an incidence angle of approximately 25° . The DEM shows a flat northern area with

very low slopes and a mountainous (volcanic) southern area with variable slopes up to 25° .

Due to the topography, the local incidence angle is largely variable in the southern area, whereas it is almost constantly equal to 25° in the northern area. SAVERS correctly simulates smaller incidence angles along the mountain slopes facing the transmitter as well as higher angles along the slopes facing the receiver. The local scattering angle map shows a clear background radial pattern, due to the nadir looking geometry of the receiver. The facets near the receiver are observed with smaller angles than the distant facets. Around the SP, the incidence and scattering angles are similar. The radial scattering angle pattern becomes noisy in the southern area, where the angle decreases along the mountain slopes facing the receiver and increases on the other opposite side of the relief.

As the local angles are known, the following scattering amplitude can be calculated for each facet in its own reference system using the electromagnetic model described in Section II-C and -D

$$\mathbf{F}' = \begin{bmatrix} F'_{vv} & F'_{vh} \\ F'_{hv} & F'_{hh} \end{bmatrix}. \quad (6)$$

In order to solve (1), the integral should be performed in a unique reference system. For this reason, the scattering amplitude from each facet in the FLR system should be transformed back to the corresponding scattering amplitude in the SGR frame, \mathbf{F}_{pq} . This can be accomplished through the polarization rotation given by the transformation in [28]

$$\mathbf{F}_{pq} = \sum_{p_{sl}} \sum_{q_{il}} \mathbf{F}'_{pq} (\hat{p}_s \cdot \hat{p}_{sl}) (\hat{q}_{il} \cdot \hat{q}_i) \quad (7)$$

where \hat{p}_s and \hat{p}_{sl} are the scattering polarization unit vector in SAVERS and the facet reference frame (both expressed in the SGR coordinates), respectively; \hat{q}_i and \hat{q}_{il} are the incident polarization unit vector in SAVERS and the facet reference frame, respectively. They can be vertical \hat{v} and horizontal \hat{h} . The formula (7) is demonstrated in the appendix. Note that vectors with the prime superscript are defined in the FLR frame, while vectors with subscript l are vectors of the facet local frame but expressed in the SGR coordinates. The FLR linear (i.e., horizontal and vertical) polarization vectors in the SGR coordinates are

$$\begin{aligned} \hat{h}_{il} &= \frac{\hat{z}_l \times \hat{l}}{|\hat{z}_l \times \hat{l}|}, & \hat{v}_{il} &= \hat{h}_{il} \times \hat{l}, \\ \hat{h}_{sl} &= \frac{\hat{z}_l \times \hat{s}}{|\hat{z}_l \times \hat{s}|}, & \hat{v}_{sl} &= \hat{h}_{sl} \times \hat{s} \end{aligned} \quad (8)$$

with $\mathbf{z}_l = \mathbf{U}^{-1} \mathbf{z}'$. Once the scattering amplitude is available, the bistatic scattering coefficients at circular polarization are

$$\begin{aligned} \sigma_{LR} &= \pi |\mathbf{F}_{VV} - \mathbf{F}_{HH} - \iota (\mathbf{F}_{VH} + \mathbf{F}_{HV})|^2 \\ \sigma_{RR} &= \pi |\mathbf{F}_{VV} + \mathbf{F}_{HH} - \iota (\mathbf{F}_{VH} - \mathbf{F}_{HV})|^2. \end{aligned} \quad (9)$$

Finally, the bistatic scattering coefficients in the SGR system can be integrated inside (1). It might occur that due to the local orientation of a facet, either the local incidence angle or the local scattering angle (or both) is larger than 90° . This means

that the facet is actually not illuminated by the transmitter or not observed by the receiver. In this case, the facet is not included in the computation of the reflected signal.

C. Soil Scattering

SAVERS can simulate the coherent and incoherent scattering amplitude. For the sake of clarity, hereafter the coherent component represents the contribution of the specular or quasi-specular reflections from the individual mean facets, possibly attenuated by the vegetation. Possible loss of coherence due to the satellite motion is not considered here. The incoherent component is due to the small scale soil roughness and to the volume scattering (including multiple scattering) from the vegetation. The simulation of the soil coherent component is based on the assumption of a spherical shape of the wavefront impinging on the surface, according to [26]. A more general formulation and solution of the scattering problem under the Kirchhoff approximation was developed for SAVERS. This new approach allows the characterization of the specular and quasi-specular scattering generated in bistatic radar systems, both inside and outside the plane of incidence, not limiting the scattering around the nadir direction as in [26]. The approach is described in detail in [22] and it proposes a characterization of the coherent normalized radar cross section (NRCS) for the radar equation and its angular pattern, as conventionally done for the incoherent component, i.e., adding the power from different surface facets. This method is particularly suitable when the simulations involve large and inhomogeneous areas, as it is the case for space-borne GNSS-R. Comite *et al.* [22] obtained a closed-form expression for the scattered field and the corresponding coherent bistatic NRCS and validated it against a numerical evaluation of the Kirchhoff integral. It is a very efficient solution, although approximated, to deal with the coherent scattering from the DEM facets and to model its angular pattern, as a coherent model should work at the scale of fractions of wavelength and would imply tremendous computational resources [19]. Moreover, it was demonstrated that the model is able to reproduce the smooth transition of the received signal as the SP moves across a boundary between two media, a feature that cannot be reproduced by a simpler geometric optics approach. However, since it models the coherent component in terms of an equivalent NRCS, it is not capable to reproduce the oscillations due to the interferences across the boundary between Fresnel zones of different order.

The incoherent scattering from the soil is modeled through the AIEM [25] following the implementation provided in [29] for the polarimetric extension to account for the circular polarization of both transmitting and receiving antennas.

The soil parameters needed as input by SAVERS are the roughness height standard deviation σ_z (this is the small scale roughness at the scale of the wavelength), the correlation length L and the soil moisture content SMC . The latter is used to model the soil dielectric constant ϵ_g through the model by Dobson *et al.* [30]. An exponential autocorrelation function is assumed.

Fig. 3 shows the LR polarized coherent and incoherent bistatic scattering coefficient computed by SAVERS over the same area and with the same configuration of Fig. 2. For this simulation, it

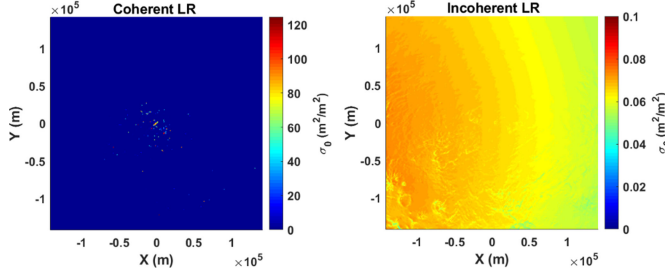


Fig. 3. Bistatic scattering coefficient for LR polarization over the same simulation area of Fig. 2: coherent (left) and incoherent (right). A bare soil with $SMC = 5\%$ and $\sigma_z = 3.5$ cm is considered. Note that the coherent contributions are restricted in very small areas.

was assumed that the soil moisture is equal to 5%, σ_z to 3.5 cm, and correlation length L to 5 cm. Due to the inhomogeneity of the surface in terms of topography, the coherent scattering consists of the contribution of several small patches mainly located around the nominal SP. All these patches are in near specular conditions, though in some cases they are far from the nominal SP. The bistatic scattering map on the right of Fig. 3 shows that the incoherent scattering is much lower than the coherent component but, as expected, it extends over a wider area.

D. Vegetation Over a Sloped Terrain

The electromagnetic model developed at Tor Vergata University [27], [31] is used by SAVERS to simulate the attenuation and scattering properties of the vegetation cover. It is a discrete scattering model based on the radiative transfer theory, which performs the Matrix Doubling algorithm [32] in order to include multiple scattering effects of any order taking place between vegetation elements and terrain. The attenuation of the soil coherent scattering increases with the vegetation biomass. For high values of biomass, the soil component is largely attenuated and becomes comparable to (or even lower than) the vegetation volume scattering. In this condition, the vegetation is a source of a significant component of incoherent scattering [15], [24], [33].

The Tor Vergata model can simulate the scattering and attenuation of several kinds of vegetation cover. This study focused on the forest case. The tree canopy is schematized as a three-layer medium: the top layer containing leaves and branches, the middle layer containing the vertical trunks, and the bottom layer representing the underlying rough soil. The leaves are represented by randomly oriented disks and the trunks by vertical cylinders.

In this study, the model was improved to account for a sloped terrain under the vegetation cover. In this situation, the propagation path through the vegetation differs from the case of flat terrain, as it is shown in Fig. 4. The branches in the crown layer maintain their orientation distribution regardless of the ground tilt. Therefore, we assumed that the scattering from the top canopy layer in the presence of topography remains the same as for a flat terrain. When a slope is present, the crown thickness along the propagation path is different [34]; this effect needs to

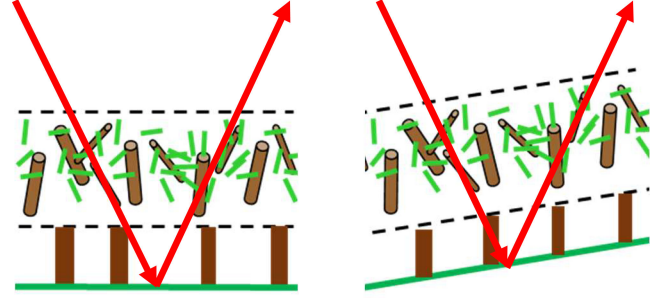


Fig. 4. Propagation paths through the vegetation over a flat and sloped terrain.

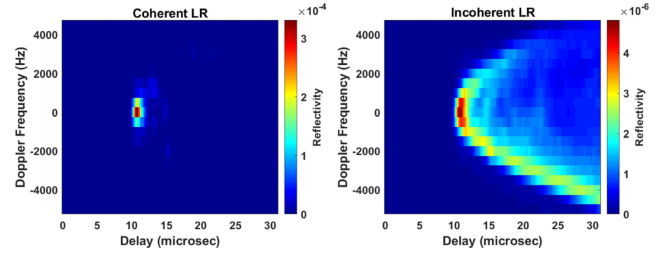


Fig. 5. DDM for LR polarization over the same simulation area of Fig. 2: coherent (left) and incoherent (right).

be included in the modeling of crown attenuation. In this version of SAVERS, it is possible to compute the correct path through the vegetation as the local incidence and scattering angles are computed for each facet of the simulation grid.

E. SAVERS Outputs

Once the signal received by the down-looking antenna is computed, as shown in (1), SAVERS provides as output the normalized DDM (nDDM) that represents the power ratio of the signals received by the down-looking antenna and that received by the up-looking antenna, assuming the same coherent integration time

$$nDDM(\tau, f) = \frac{|Y_{rt}(\tau, f)|^2}{|Y_{RR}^{UP}|^2}. \quad (10)$$

The correlator output of the up-looking antenna Y_{RR}^{UP} is defined as follows

$$|Y_{RR}^{UP}|^2 = \frac{\lambda^2}{(4\pi)^2} P_T T_i^2 \frac{G_T(\vartheta_i) G_R^{UP}(\vartheta_i)}{R_{TR}^2}. \quad (11)$$

R_{TR} is the distance between the transmitter and the receiver and G_R^{UP} is the up-looking antenna gain pattern. Note that the normalization of the up-looking correlator output allows overcoming the dependence on possible nondimensionless constant factors resulting from the formulations in [9] and [10].

Fig. 5 shows an example of SAVERS output, the DDM obtained by solving (1) and (10). Both the coherent and the incoherent component are reported in the figure for the LR polarization case. These normalized DDMs have been obtained for the same area and with the same configuration as of Figs. 2 and 3. As expected, the incoherent component shows a typical

horseshoe shape that spreads in delay and Doppler, while the coherent component is very concentrated in a small area of the map. In this simulation, the magnitude of the incoherent component is much lower than the coherent one. The origin of the SGR system (i.e., the nominal SP) is also the reference point of Doppler and delay. In the DDM, the SP is always set to zero Doppler and to 15 μs delay. This setting assures to always show the DDM peak in the figure. Due to the topography effects, indeed, the area contributing to the DDM peak might be shifted with respect to the nominal SP and, therefore, it might have a different Doppler and delay.

III. COMPARISON WITH MEASUREMENTS

The performance of the upgraded version of SAVERS was evaluated over a bare area with a complex topography, such as that of Tibesti volcanic region in Chad, and over an open forest located in southern Congo. In order to validate the simulator outputs, several acquisitions of TDS-1 were selected over these study areas, and SAVERS inputs were set according to the real observation geometry, antenna gain, and delay-Doppler sampling of the selected TDS-1 data. The simulated and observed DDM and peak reflectivity were then compared.

A. TDS-1 Data

The TDS-1 satellite mission, developed by Surrey Satellite Technology Ltd and launched in July 2014, carries a GNSS-R instrument prototype, the Space GPS Receiver Remote Sensing Instrument [35]. The receiver supports the GPS L1 frequency band and provides left-hand circularly polarized DDM of the reflected signal. An up-looking low-gain antenna collects the direct signal in right-hand circular polarization. A noise collection operation mode is included both in the direct and in the reflection receiver chains. It allows estimating the receiver gain by measuring the output level produced by a noise source (black body), together with its temperature.

Data were freely available through the Measurement of Earth Reflected Radio-navigation signals By Satellite (Merrbys) portal (<http://merrbys.co.uk>) under a Creative Commons Attribution, Non Commercial 4.0 International License. In this work, the level 1b (L1b) products were used. They consist of DDM sampled every second, after a 1 ms coherent and 1 s incoherent integration, whereas the direct signal is sampled each 10 s. Details about the datasets can be found in the Product Manual available at the Merrbys website.

The TDS-1 observable used in this study, i.e., the reflectivity Γ_{TDS} , was obtained by processing the L1b data. Details on the processing are reported in [36]. Assuming that the received signal is dominated by the coherent component of the surface scattering (as shown in Fig. 3), the radar equation for the coherent signal received by the down-looking antenna can be written as

$$P_R^S = \Gamma(\vartheta) \frac{\lambda^2 G_T G_R P_T}{(4\pi)^2 (R_R + R_T)^2}. \quad (12)$$

The distance from the receiver to the SP, R_R , and from the transmitter to the SP, R_T , and the down-looking antenna gain, G_R , are provided in the L1b products. Following [36] for

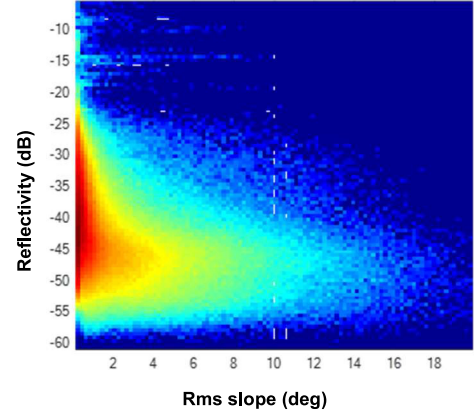


Fig. 6. Histogram of TDS-1 peak reflectivity at global scale as a function of the rms slope over a 5×5 pixel area of a 30 arcs DEM.

the computation of the transmitter Equivalent Isotropic Radiate Power (EIRP = $G_T P_T$) from the direct signal collected by the up-looking antenna, and inverting (12), the reflectivity can be expressed in terms of the peak power P_R^* of the DDM, the DDM noise N^* estimated from the delay lines preceding the peak, the direct power P_d^* and the related noise N_d^* , and the up- and down-looking antenna gains through the following formula:

$$\Gamma_{\text{TDS}}(\vartheta) = \frac{(P_R^* - N^*)}{(P_d^* - N_d^*)} \frac{G_R^{UP}}{G_R} \frac{(R_R + R_T)^2}{R_{TR}^2}. \quad (13)$$

The distance from the transmitter to receiver, R_{TR} , can be computed from the position of the satellites available in the L1b product, together with P_d^* , N_d^* and the down-looking antenna gain toward the SP. Conversely, the upward antenna gain G_R^{UP} is not provided in the L1b product, so that it was set constant and equal to its maximum value of 4 dB, being a low-gain wide-beam antenna, according to the Merrbys documentation. The TDS-1 calibration in (13) has some approximations, not only because of the poor knowledge of the antenna gain, but also because it assumes the same gain of the receiving chains of direct and reflected signals, as discussed in [36]. Moreover, the calibration of GNSS-R data depends on the accurate characterization of the transmitter EIRP, that is still a challenge due to the variations of transmit power within the GPS constellation and the uncertainties in the transmit antenna gain [37].

The TDS-1 DDMs are characterized by a delay resolution of 0.244 μs and a Doppler resolution of 500 Hz. They reach a maximum delay of 31.3 μs and have a Doppler frequency ranging from -5 to 5 KHz.

A preliminary analysis was carried out to evaluate the effect of the topography on the peak reflectivity measured by TDS-1. Fig. 6 shows the histogram of peak reflectivity observed at global scale on July 2018 as a function of the rms slope. The latter was computed over 5 by 5 pixels of a 30 arcsec DEM (the global 30 arcsec GTOPO30, doi: /10.5066/F7DF6PQS).

The plot shows a strong relationship between the topography and the measured reflectivity. Over the mountainous areas, where the rms slope is high, the reflectivity is approximately 10 to 15 dB lower than that over the flat areas. The reflectivity

over the mountains reaches values close to the noise floor. The DDMs over these areas are characterized by several low peaks spread in delay and Doppler and the identification of the main peak is unreliable. The decrease of reflectivity over the reliefs is due to the increase of the large-scale roughness, i.e., the variation of the local slope in the observed area. As explained in the previous section and shown in Figs. 2 and 3, the local slope causes a signal reflection in the local specular direction which can be significantly different from the direction toward the receiver antenna, i.e., the nominal specular direction. As a consequence, the receiver antenna in many cases is not measuring the peak of the reflected signal but a lower fraction.

To carry out the validation of SAVERS, the simulator input parameters referring to the transmitter and the receiver were set to reproduce GPS and TDS-1 characteristics at the time of the acquisition. All information about GPS and TDS-1 can be found in the L1b products, including satellite position and velocity.

The look-up table of TDS-1 down-looking antenna gain as a function of discrete azimuth and elevation angles is provided by the Merrbys website and it was given as input to the simulator. This antenna has a 13-dB gain with a 3-dB beamwidth of 30°.

Moreover, SAVERS output was made comparable to the TDS-1 observable by applying a coherent calibration, i.e., by multiplying (10) by the last two factors of (13)

$$\Gamma_{\text{SAVERS}}(\vartheta) = n\text{DDM} \frac{G_R^{UP}}{G_R} \frac{(R_R + R_T)^2}{R_{TR}^2}. \quad (14)$$

The delay and Doppler were sampled as done for the TDS-1 data. As the TDS-1 DDMs are limited to a maximum delay of 31.3 μs , the same limit was set to the SAVERS DDMs. For this reason the size of the simulation area was defined large enough to include the iso-delay line of 31.3 μs . This was done by computing the length of the major semiaxis of this isodelay line using (2) and setting the size of the simulation area equal to two times this length.

The TDS-1 tracks used for the following comparison were selected checking the high-quality flag of the available acquisitions over the study sites and considering small incidence angles to mitigate the poor knowledge of the up-looking antenna pattern.

B. Comparison Over Complex Topography

The region of the Tibesti Mountains in the central Sahara was selected as a validation site for this study. This is a volcanic area located in northern Chad and southern Libya and adjacent to Niger. The mountain range reaches an elevation of 3400 m, it includes five volcanoes and several plateaus, and it is surrounded by relatively flat areas. The region is mainly bare, and the monsoon season is highly variable from year to year. The complex topography in a dry and bare area makes this an ideal site to improve the understanding of the TDS-1 reflectivity measurements and to validate SAVERS simulations in a real environment. Fig. 7 shows the location of the validation site and the TDS-1 SP tracks used in this study overlying the Shuttle Radar Topography Mission (SRTM) DEM of the Tibesti region.

Five descending tracks were selected among the TDS-1 data collected over this region: two passing over the mountain range

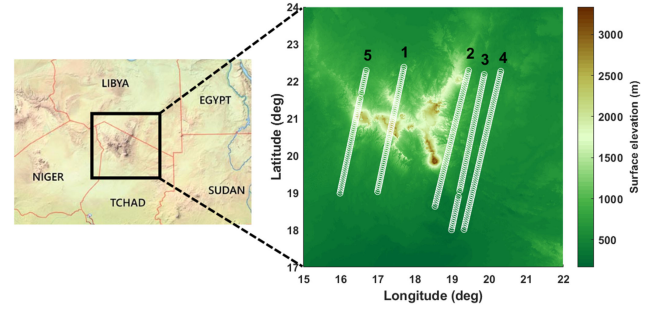


Fig. 7. Map of the Tibesti region in Chad (left) and location of the TDS-1 SP tracks overlying the SRTM DEM (right).

(no. 1 in November 2016 and no. 5 in January 2017), one at the foot of the range (no. 2 in May 2017), and two over the flat areas (no. 3 in April 2017 and no. 4 in November 2016). All these tracks, except one, are characterized by a nominal incidence angle ranging from 20° to 24° and the track no. 4 by a nominal incidence angle from 11° to 16°.

In order to carry out the validation of SAVERS over the Tibesti region, the corresponding settings of the TDS-1 acquisitions were given as input, i.e., transmitter and receiver position and velocity along the track. The soil moisture and soil roughness were selected in a realistic range for a dry and volcanic area, i.e., SMC = 5% and $\sigma_z = 3.5$ cm were assumed.

The SRTM DEM was given as input to the simulator to compute surface elevation, slope, aspect, and local angles for each facet of the simulation area (the DEM was downloaded from the website <https://cgiarcsi.community/data/srtm-90m-digital-elevation-database-v4-1/>). To evaluate the effect of the simulation resolution on the output accuracy, a test was carried out running SAVERS for a resolution of the simulation grid of 100, 300, and 1000 m. For this scope, the 30 arcsec SRTM DEM was interpolated on the simulation grid with a resolution of 1000 m, whereas the 3 arcsec SRTM DEM was interpolated at resolutions of 100 and of 300 m. The resolution test was carried out for the track no. 1 of Fig. 7, assuming a homogenous soil moisture and soil roughness along the whole track, equal to 5% and 3.5 cm, respectively. Peak reflectivity patterns and DDMs simulated by SAVERS at the three resolutions were compared with the TDS-1 data. Fig. 8 shows the comparison among the peak reflectivity patterns observed and simulated along the track no. 1. The surface elevation obtained from the 3 arcsec SRTM DEM and the average of the slope in a window of 5×5 pixels around the nominal SP are reported in the plot, as a topography reference along the track. SAVERS can correctly reproduce the variations of the reflectivity along the track due to the topography at all resolutions. The reflectivity observed over the mountains is approximately 10 to 15 dB lower than the reflectivity over the flat areas at the beginning and end of the track. In the areas where the slope is higher and more variable, the reflectivity reaches the lowest values.

The decrease of the simulation resolution worsens the agreement with the observations. The 1-km resolution does not provide information about slope and aspect accurate enough to correctly simulate the contribution of each facet to the total

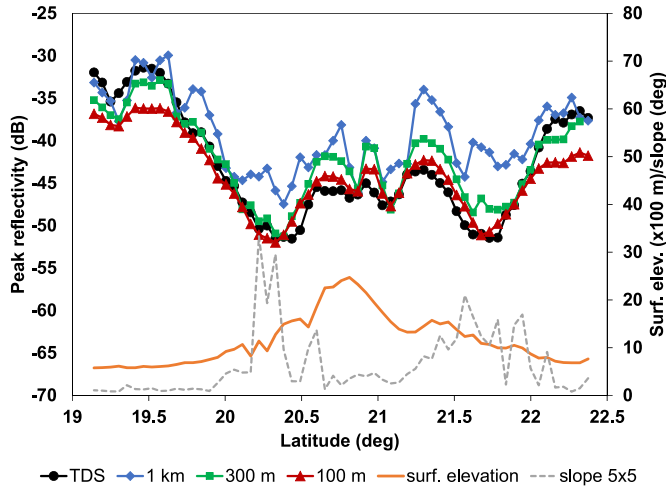


Fig. 8. Simulated and observed peak reflectivity vs latitude of the track n°1. Comparison of the results at three simulation resolutions: 1 km, 300 m, and 100 m.

reflectivity, leading to a noisy and unstable pattern (the correlation coefficient between simulated and measured reflectivity R^2 is 0.74 and the root mean squared error, RMSE, is 5.1 dB). Simulations with 300- and 100-m resolution lead to more accurate patterns along the track, with $R^2 = 0.90$ and RMSE = 2.5 dB for both cases. At 100-m resolution, the peak reflectivity is underestimated over the flat area and slightly overestimated over the mountains. These discrepancies can be explained by possible variations of the small scale surface roughness along the track. The simulations assume a homogenous roughness in the region; it would be more realistic to assume a smoother surface over the flat areas than over the mountains.

Increasing the resolution, keeping unchanged the other inputs, the peak reflectivity values decrease. This effect is mainly due to the slope distribution of all facets in the simulation area derived from DEM's with different resolution. At higher resolution, many more facets of the simulation area have high slope, so that the chance to find facets in the nominal specular condition (signal reflected in the direction of the receiver) is lower. Therefore, the coherent component and the total signal reflected toward the receiver are lower at 100-m resolution than at 1-km resolution.

The effect of the simulation resolution on the DDM was evaluated as well, in terms of shape and peak position. Two examples are shown in Figs. 9 and 10, reporting the TDS-1 normalized DDM observed at 20.22° latitude and at 21.89° latitude along the no. 1 SP track, respectively, and the corresponding simulated normalized DDMs at three different resolutions. The normalizations carried out in (13) and (14) for the peak values were repeated for all the points of the TDS-1 DDM and SAVERS DDM, respectively. Moreover, all DDMs are normalized to the peak value reported on top of each map.

In both cases, the peak reflectivity position in the DDM is wrongly simulated when running the simulator at a resolution of 1 km. Therefore, the 1-km resolution is the worst choice over areas with a complex topography. The two figures show that the best result is obtained with a resolution of 100 m, when the

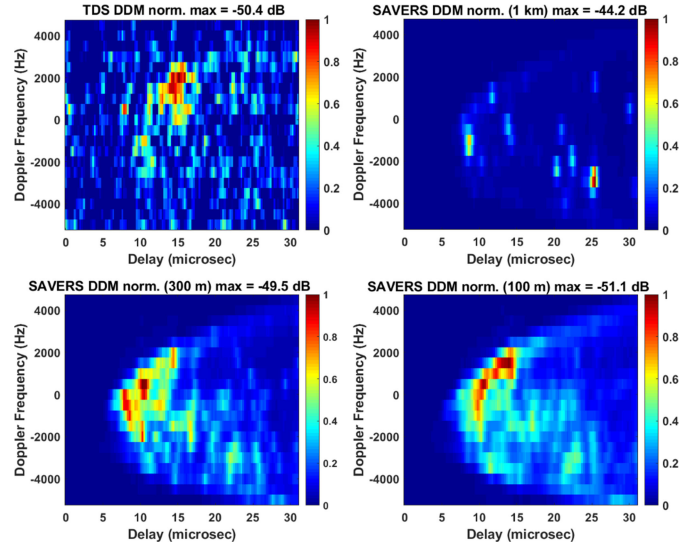


Fig. 9. Comparison of normalized DDM for SP at 20.22° latitude: observed (top-left), simulated at 1-km resolution (top right), simulated at 300-m resolution (bottom left), simulated at 100-m resolution (bottom right).

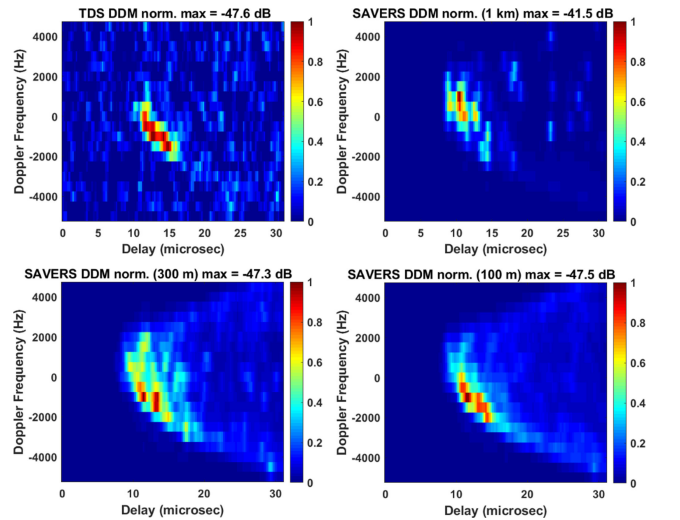


Fig. 10. Comparison of normalized DDM for SP at 21.89° latitude: observed (top-left), simulated at 1-km resolution (top right), simulated at 300-m resolution (bottom left), and simulated at 100-m resolution (bottom right).

simulated peak is approximately at the same delay and Doppler observed by TDS-1.

Along the entire selected track, the accuracy in simulating the peak shift caused by the topography effect is, in general, comparable for the 100- and 300-m resolution cases. Only a few SPs along the track show an evident difference of peak positions between the two sets of simulations, including that reported in Fig. 9. The mean absolute difference between the observed and simulated Doppler of the peak, computed over the entire track no. 1, is approximately 600 Hz at 100-m resolution and approximately 540 Hz at 300-m resolution. The mean absolute difference between TDS-1 and SAVERS delay of the peak is approximately 1.5 μ s at both resolutions. In conclusion, the two highest resolutions lead to a similar error in the simulation of the

peak position. However, considering that increasing the simulation resolution implies to significantly increase the number of facets on which the electromagnetic model must run, a resolution of 300 m is the best compromise to limit the simulation time and to reach a good accuracy of SAVERS outputs.

Concerning the shape of the DDM, the use of higher resolutions leads to a better agreement between simulations and observations around the peak. The TDS-1 DDMs are affected by noise and the values under the noise threshold are filtered out (dark blue bins). As the DDMs tails are characterized by a weak reflectivity, they are often hidden under the noise. Whereas, no noise was added to the simulations and the DDMs tails are clearly visible. Due to the decrease of the peak for higher resolutions and the normalization to the maximum value, the tails are more evident at 100- and 300-m resolution than at 1 km.

It is worth mentioning that Figs. 9 and 10 show an evident topography effect that determines the shift of the DDM peak along the Doppler frequency axis. The DDMs of both figures refer to nominal SPs located at the foot of the mountain range, at 20.22° and 21.89° latitude, respectively (see Fig. 7). In both cases, the TDS-1 acquisitions were carried out along a descending orbit. However, in the case of the point at 20.22° latitude (see Fig. 9) the receiver was leaving the mountain range, i.e., the mountains were located in the direction opposite to the receiver velocity. Whereas at the time of the acquisition at 21.89° latitude (see Fig. 10), the receiver was moving toward the mountain range. The TDS-1 DDMs show that the main contribution to the scattering does not come from the nominal SP (at zero Doppler) but from the points located along the slope of the reliefs. When the mountain slope is located backward the nominal SP along the track, the main contribution to the scattering occurs at negative Doppler frequencies, as in Fig. 9. When the slope is located forward the nominal SP along the track, the main contribution to the scattered signal occurs at positive Doppler frequencies, as in Fig. 10. SAVERS is able to correctly reproduce this topography effect when the simulation is carried out on a high-resolution grid.

In order to further analyze the SAVERS performance over a complex topography, the simulator was run for all TDS-1 passes over the Tibesti Mountains shown in Fig. 7. As for the case of track no.1, position and velocity of transmitter and receiver were read in the TDS-1 data, the gain pattern of TDS-1 down-looking antenna was included in the simulator, the soil moisture was set to 5% and the soil roughness to 3.5 cm. For all tracks, the general pattern of TDS-1 reflectivity is well estimated by SAVERS over both flat areas and mountains. The scatter plot between the observed and simulated peak reflectivity is shown in Fig. 11. The comparison of the peak values results in $R^2 = 0.55$ and RMSE = 3.9 dB.

A clear overestimation was found in some areas away from the mountain range. As mentioned before, most of the discrepancies can be justified by the uncertainties in the surface roughness, as well as in other surface parameters. The soil moisture and the soil texture could be affected by the large elevation variation and by the distance from the volcano's crater. Nevertheless, the validation results confirm that the upgraded version of SAVERS

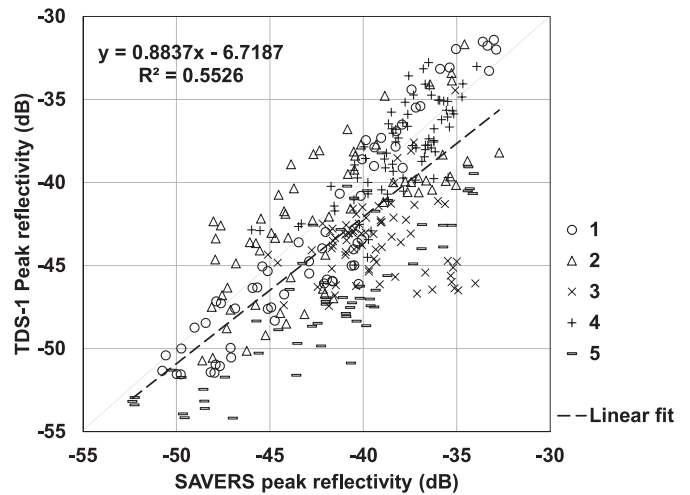


Fig. 11. Scatter plot of observed vs. simulated peak reflectivity.

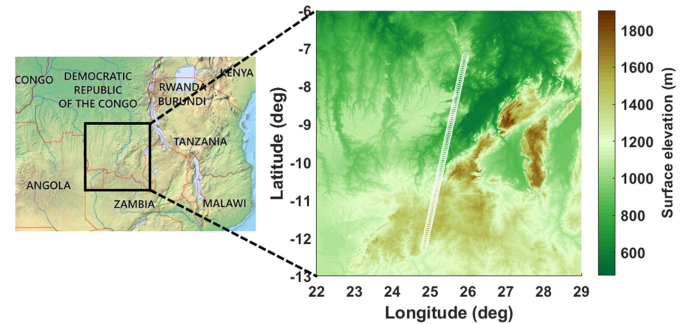


Fig. 12. Map of southern Congo (left) and location of the TDS-1 SP track overlying the SRTM DEM (right).

presented in this study can correctly describe the topography effects over bare soils.

C. Comparison Over Forested Areas

A region in the South of the Democratic Republic of Congo and in the North of Zambia were selected in order to validate SAVERS over surfaces covered by forest (the black rectangle in Fig. 12). The selected area is characterized by a gentle topography with a surface elevation ranging from 600 to 2000 m. As reported in the land cover map provided by the International Geosphere-Biosphere Programme, this region is largely covered by open forest and woodland with some patches of dense forest. Lakes and rivers are present, as well. The southern part of the region is characterized by low vegetation and bare soils.

The performance of SAVERS was tested for the TDS-1 track collected in February 2017 (PRN 28), shown in Fig. 12 overlying the SRTM DEM. Fig. 13 reports the peak reflectivity observed by TDS-1 along the selected track. As an indicator related to the vegetation biomass, the tree height estimated from ICE-GLAS LiDAR data collected from the International Space Station [38] is included in the plot. Except the two peaks around -8.9° and -11.4° latitude, the reflectivity observed by TDS-1 has a variability range of approximately 10 dB, from -43 to -33 dB. The LiDAR tree height shows an inhomogeneity of

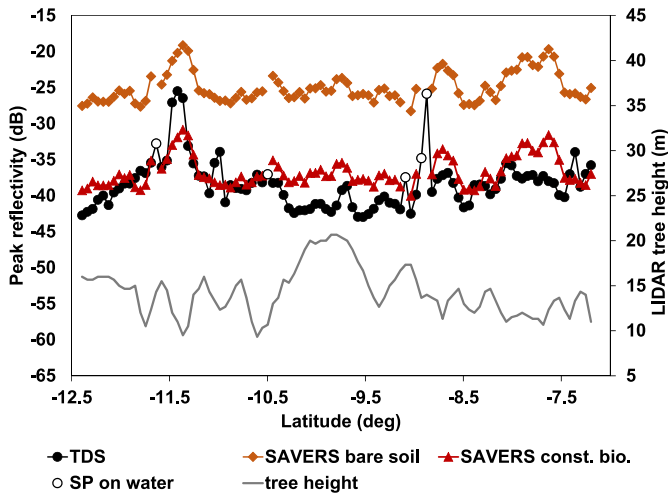


Fig. 13. Peak reflectivity observed by TDS-1 along the track of Fig. 12 (black circle); SAVERS reflectivity simulated assuming a bare surface (brown diamond) and a constant biomass of 85 t/ha (red triangle); the reported tree height has been estimated by LiDAR.

the vegetation along the track. In particular, the area between -10.2° and -9.6° latitude is characterized by taller trees and probably a higher biomass than the rest of the track. For this reason, the reflectivity observed by TDS-1 is slightly lower at these latitudes than in other areas. The peak at -11.4° latitude corresponds to a minimum of tree height, which is likely due to the presence of a very low biomass or bare surface.

Some SPs along the track are located within or near water bodies. These points are reported in Fig. 13 with empty circles. The presence of water (namely, of a strong reflection from a smooth surface) causes the peak in the reflectivity pattern around -8.9° latitude. In principle, SAVERS can account for the presence of a water body by setting the suitable values of dielectric constant and surface roughness. However, SAVERS cannot simulate the oscillations occurring when the SP and the first Fresnel zone are near the boundary between water and land, as discussed in [22]. This could lead to nonnegligible errors in the retrieval of small inland water extent, as pointed out in [39].

As the analysis here is focused on the simulations over forested areas, the SPs within or near the water bodies were disregarded and SAVERS was run assuming the presence of a homogeneous woodland.

The soil and the vegetation parameters were selected in realistic ranges for the region of Congo-Zambia. They were set to the following values: SMC = 15%; $\sigma_z = 2.2$ cm; mean diameter at breast height (dbh) and its standard deviation equal to 12 and 5 cm, respectively; log-normal dbh distribution; tree density equal to 150 trees/ha; LAI = $5 \text{ m}^2/\text{m}^2$; allometric equations by [40]. Following the indication given in Section III-B, the simulations were carried out at a resolution of 300 m, using the 3 arcsec SRTM DEM. The forest above ground biomass was assumed to be homogeneously equal to 85 t/ha along the track. The simulated peak reflectivity is compared to the observations in Fig. 13. To better evaluate both the effect of the topography and the forest attenuation on simulations and observations, SAVERS

was first run excluding the presence of forest (same inputs parameters but biomass set to zero).

The simulated pattern for a bare soil reported in Fig. 13 shows that, though gentle, the topography clearly affects the reflectivity, causing variations in a range of approximately 10 dB. Several features of the TDS-1 reflectivity pattern correspond to features of SAVERS reflectivity pattern over bare soils. Likewise, when the forest is taken into account, the simulated pattern is still largely due to the topography effect, but now the soil surface component is attenuated by the vegetation. The peak in the TDS-1 pattern around -11.4° latitude can be now explained by a combination of the effect of the topography and low vegetation.

The peak reflectivity simulated along the track assuming the presence of forest is smoother than the observed one, as it underestimates the higher reflectivities and overestimates the lower reflectivities, with an $R^2 = 0.36$ and an RMSE = 3.2 dB. However, this might be due to the uncertainties on the above ground biomass and to the inaccurate assumption of a homogeneous biomass along the track, which is not supported by the tree height data.

To overcome this issue, more accurate estimates of variable biomass along the track were given as input to the simulator. The biomass estimates were obtained by following two approaches. The first approach consisted of retrieving the biomass from the tree height using a regression function. Specifically, a third-degree polynomial was found to link the LiDAR tree height to the biomass estimated from the allometric equations in [40] applying the procedure described in [41] to find the tree height. A second biomass estimate was obtained from the pan-tropical biomass map by Avitabile *et al.* [42].

Firstly, the simulator was run considering for each SP the biomass estimated from the tree height. The result is shown in Fig. 14 (top). SAVERS overestimates the reflectivity with an average bias of 3.6 dB. This might be probably corrected by using allometric equations more specific for this test site. However, the simulated pattern is in good agreement with that observed, holding $R^2 = 0.55$ and unbiased RMSE = 2.2 dB.

Secondly, the simulator was run giving as input the biomass from the map in [42] and the results are shown in Fig. 14 (bottom). As this biomass varies in a large interval reaching very low values along the track, the corresponding simulated reflectivity has a larger variability range than the observed one. For this reason, the largest reflectivity values observed by TDS-1 at -11.4° latitude can be better simulated using the biomass map in [42]. From approximately -7° to -9° latitude, both estimates of biomass are too low and, consequently, the simulated reflectivity is overestimated. Whereas the higher biomass estimates from approximately -9° to -10° latitude allow to enhance the decrease of the reflectivity simulated in this area, with respect to using a constant biomass. It is worth to remark that both LiDAR height data and maps in [42] are not simultaneous to the TDS-1 measurements.

Although the reference data are unfortunately not enough accurate and in some cases contradictory, the results over forest are encouraging. They demonstrate that SAVERS can correctly simulate the reflectivity variations due to the biomass inhomogeneity and to the underlying topography.

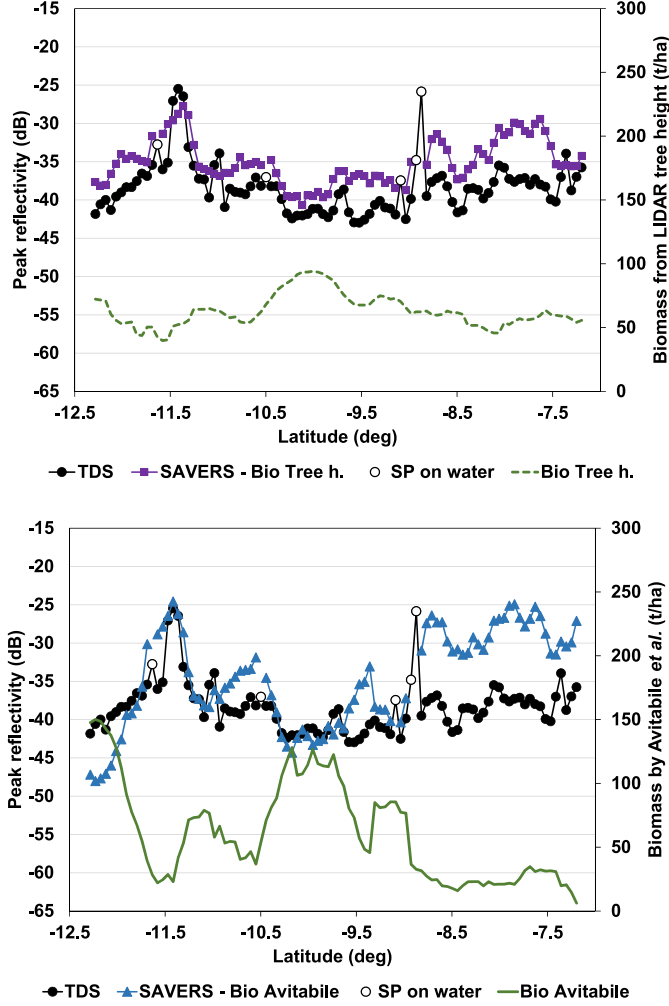


Fig. 14. Simulated and observed peak reflectivity vs. latitude along the track of Fig. 12, and the variable above ground biomass given as input. Top: biomass estimated from LiDAR tree heights; bottom: biomass from [42].

IV. SENSITIVITY ANALYSIS

One of the main applications of models is the possibility to carry out a sensitivity analysis. Indeed, models can single out the effects of the main variables involved in the simulation process and weigh their impact on the remotely sensed observable. Therefore, SAVERS was used to perform a sensitivity analysis of the space-borne GNSS-R signal to soil moisture and forest biomass, in case of a flat terrain and in the presence of topographic reliefs. The sensitivity analysis consisted of varying one parameter at a time in a selected range, keeping fixed all the others, and of evaluating the corresponding variations of the simulator outputs.

A. Soil Moisture in Flat and Sloped Terrains

The sensitivity of the LR reflectivity to SMC was evaluated assuming the GNSS-R system settings of TDS-1 acquisitions (but with a generic cosinusoidal pattern for the down-looking antenna gain). The SMC ranged between 5% and 40% (from very dry to very moist soil conditions), whereas the other inputs

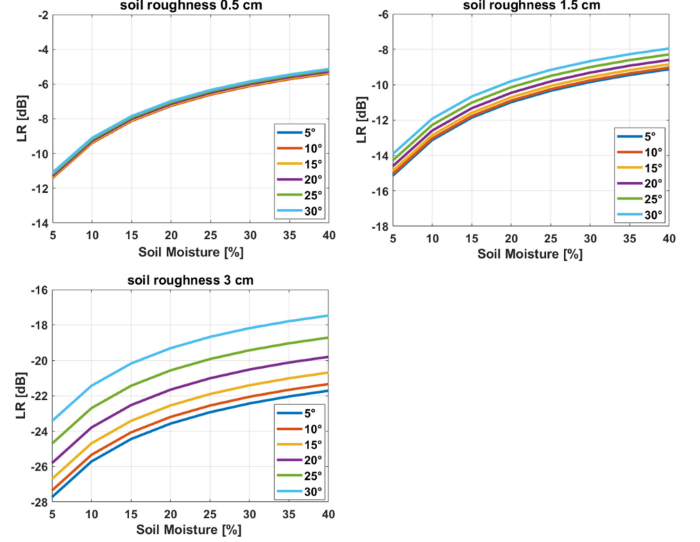


Fig. 15. Simulated reflectivity at LR polarization vs. SMC of a flat terrain for three small scale roughness: 0.5 cm (top left), 1.0 cm (top right), and 3 cm (bottom). Colors correspond to different incidence angles.

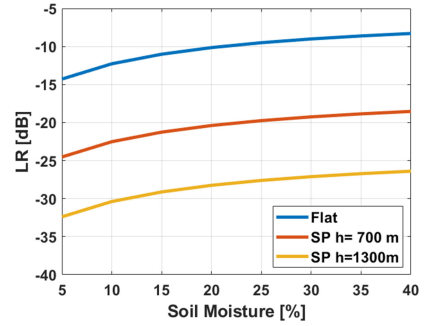


Fig. 16. Simulated reflectivity at LR polarization vs. SMC for three surface elevations h : 0 m (flat), 700 m, and 1300 m (DEM of Fig. 7). Soil roughness was set to 1.5 cm and incidence angle to 25°.

parameters were kept constant. The same analysis was repeated for several values of incidence angle (from 5° to 30°) and for three surface roughness values (0.5, 1.5, and 3 cm). The results are reported in Fig. 15. In case of a flat terrain, the simulations indicate an average sensitivity of about 1.5 dB for a 10% variation of SMC (slightly higher for low SMC and slightly lower for high SMC). This sensitivity is independent of the incidence angle and of the small scale roughness. The sensitivity is slightly higher than that found in [43] where an increase of the reflectivity of approximately 1 dB was found for a 10% increase of SMC.

To investigate the topography effects on the sensitivity to soil moisture, two SPs at a different elevation, 700 and 1300 m, were selected along the track no.1 in Fig. 7. SAVERS was run with the system configuration of these two points varying the SMC and assuming constant soil roughness and incidence angle (1.5 cm and 25°, respectively). Fig. 16 shows the obtained LR reflectivity and, as a reference, the corresponding reflectivity over a flat terrain. Though the LR reflectivity decreases at high surface elevation, the sensitivity to SMC is independent of the topography.

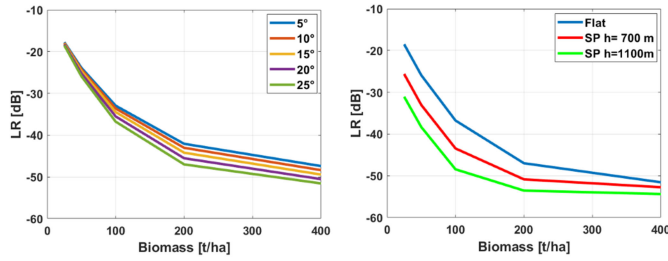


Fig. 17. Simulated reflectivity at LR polarization vs. forest biomass, for 1.5-cm soil roughness and 25% soil moisture. Left: forest over a flat terrain. Colors correspond to different incidence angles. Right: forest over a real DEM and incidence angle set to 25°. Colors correspond to different surface elevations: 0 (flat), 700, and 1100 m.

It is important to underline that the sensitivity to soil moisture is not much affected by incidence angle, small scale roughness, and surface elevation, but the reflectivity value is strongly dependent on the topography. Therefore, algorithms for large scale retrieval of soil moisture should first take into account the topography before any further analysis.

B. Forest Biomass in Flat and Sloped Terrains

The forest biomass introduces attenuation on the coherent specular scattering of the underlying soil. However, since the latter is very large, forests do not completely mask the coherent reflection from soil at L-band. As far as the attenuated coherent soil contribution is larger than the incoherent scattering from the vegetation volume and from the soil, the GNSS-R signal shows a significant sensitivity to biomass. This allows forest monitoring within a wider biomass range with respect to the monostatic radar. At L-band it is generally observed that there is a variation of the backscattering coefficient with biomass till values in the order of 100 t/ha [44]. The left plot in Fig. 17 reports an example of the GNSS-R sensitivity to forest biomass for the case of a flat surface. The analysis was carried out varying the biomass from 25 to 400 t/ha. The biomass variation is linked to a variation of the mean dbh from 7 to 21 cm, of the tree density from 100 to 300 trees/ha and LAI from 0.5 to 8 m²/m². The Jenkins allometric equations and the log-normal dbh distribution were used. The soil roughness was set to 1.5 cm and the soil moisture to 25%. The analysis was repeated for incidence angle values varying from 5° to 25°.

The LR reflectivity is clearly sensitive to biomass increases. A total decrease of approximately 45 dB is simulated for a total increase of biomass of 375 t/ha. The sensitivity is independent of the incidence angle. The results obtained by SAVERS simulations are in agreement with those obtained from experimental airborne campaigns reporting a sensitivity of about 1.5 dB for a biomass variation of 100 t/ha [6], [45].

The effect of the topography on the GNSS-R sensitivity to biomass was further investigated by repeating the same analysis over an area characterized by a relevant large scale roughness. The area of Fig. 7 was assumed to be covered by forest (having the same parameters used for the analysis over a flat surface) and two SPs were selected along the track no. 1 at a DEM elevation of

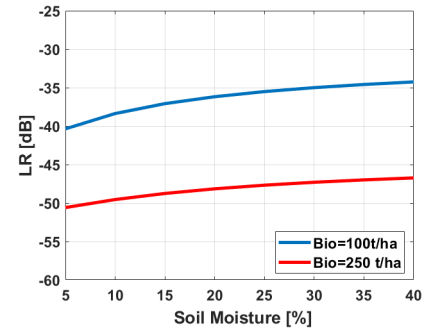


Fig. 18. Simulated reflectivity at LR polarization vs. soil moisture content over a flat forested area for two biomass values: 100 t/ha and 250 t/ha. Soil roughness was set to 1.5 cm and incidence angle to 25°.

700 and 1100 m. SAVERS was run for these two points assuming a soil roughness of 1.5 cm and a soil moisture of 25%. The right plot of Fig. 17 shows the sensitivity curves for the two points, as well as that for the flat surface case. The curves refer to a nominal incidence angle of 25° with respect to the ellipsoid.

The sensitivity to biomass decreases over areas with a significant topography. When the topographical elevation increases, the reflectivity decreases and it reaches a saturation at biomass values of approximately 200 t/ha. This probably occurs because in areas with complex topography the coherent specular reflections from the DEM facets become weak, as discussed before, and comparable to the incoherent scattering of the vegetation volume and of the soil. The latter contributions lead to saturation, as in the monostatic configuration.

Finally, the sensitivity of the GNSS-R reflectivity to soil moisture over areas covered by a forest was investigated. A flat surface was assumed for this analysis. The soil small-scale roughness was set to 1.5 cm and the nominal incidence angle to 25°. The soil moisture was varied in the range from 5 to 40%. The analysis was repeated for two cases of forest biomass, 100 and 250 t/ha. The results reported in Fig. 18 show that the reflectivity is sensitive to soil moisture variations. However, the sensitivity (dB's per 10% variation of soil moisture) decreases from 1.5 dB/10% for the bare surface case to 1 dB/10% for a forest with 100 t/ha biomass and to 0.5 dB/10% for a forest with 250 t/ha biomass. Note that the variation of reflectivity due to the forest is higher than that due to the full range of soil moisture, which means that ancillary information about vegetation is essential to set up any retrieval of moisture.

V. CONCLUSION

An upgraded version of SAVERS, suitable to simulate GNSS-R signals received by space-borne sensors, was presented and validated in this article. The current version of the simulator processes the information provided by a DEM of the observed area to estimate the signal reflected by a surface with a variable topography. Known the local elevation, slope, and aspect, SAVERS computes the local incidence and scattering angles and local scattering amplitudes. This allows identifying the facets in the observed areas that mainly contribute to the reflected signal, being in near-specular conditions. The contributions of all facets,

dependent on moisture, small scale roughness, and superimposed vegetation properties, are then properly weighted according to the polarization rotation and the down-looking antenna pattern and finally integrated. The facet biogeophysical properties are not necessarily homogeneous within the integration area corresponding to the DDM range and Doppler extension.

The simulator was validated against TDS-1 data over the volcanic region of Tibesti in Chad, with bare surface and complex topography, and over an open forest in southern Congo with gentle reliefs. It was found that the reflectivity received over the reliefs (i.e., where the surface slope is largely variable) is lower than that of flat areas. The simulations are in good agreement with the observations over both sites. Along the entire TDS-1 track passing over the Tibesti region, SAVERS correctly estimated the strong effect of the topography on the DDM shape and the peak reflectivity value and its variation along the track. The attenuation of the forest combined to the effect of the large scale surface roughness is also correctly simulated by SAVERS along the TDS-1 track over Congo, although the reference data on the biomass were not very accurate.

The main factors that affected the agreement with the observations were the simulation resolution and the spatial variability of surface and vegetation parameters along the simulated track. It was shown that the simulation resolution (i.e., the size of each facet) was an important factor affecting the simulation accuracy. It was concluded that a resolution of 300 m was a good compromise to obtain accurate results with a reasonable simulation time. Moreover, taking into account the spatial variability of surface roughness and vegetation parameters, such as biomass, the agreement with the observations could be improved.

The simulator was further used to carry out a sensitivity analysis of the GNSS-R signal to soil moisture and forest biomass over both flat areas and complex topography. The sensitivity to soil moisture is not affected by the topography, though the reflectivity value decreases significantly over the reliefs. Over flat areas, the GNSS-R signal reached a saturation for biomass values larger than in the monostatic configuration. However, in the presence of reliefs, the saturation is reached for lower values of biomass. As the coherent specular reflection may become very low over a complex topography, the incoherent scattering may become predominant, thus leading to a saturation effect. However, the saturation threshold of the GNSS-R signal occurs only over high reliefs and it is higher than that of the monostatic configuration.

These considerations lead to two recommendations. Soil moisture and biomass retrieval algorithm from space-borne GNSS-R data should take into account the topography effect. Moreover, the GNSS-R instrument design should be developed considering that the signal received over mountain areas, once correctly tracked, can reach the noise threshold easier than in the case of flat areas.

APPENDIX

The incident electromagnetic field \vec{E}^i is related to the scattered field \vec{E}^s , through the scattering amplitude matrix \mathbf{F}

$$\vec{E}^s = \mathbf{F} \cdot \vec{E}^i.$$

The electromagnetic fields and the scattering matrix can be also defined in the FLR and can be expressed in the SGR coordinates

$$\vec{E}_l^s = \mathbf{F}' \cdot \vec{E}_l^i.$$

By definition

$$\mathbf{F} = \sum_{p_s} \sum_{q_i} F_{pq}(\hat{p}_s \hat{q}_i)$$

$$\mathbf{F}' = \sum_{p_{sl}} \sum_{q_{il}} F'_{pq}(\hat{p}_{sl} \hat{q}_{il}).$$

In the dyadic representation, the fields in the main reference system and the local fields are related as

$$\vec{E}^i = \sum_{q_i} \hat{q}_i \hat{q}_i \cdot \vec{E}_l^i$$

$$\vec{E}^s = \sum_{p_s} \hat{p}_s \hat{p}_s \cdot \vec{E}_l^s.$$

That is

$$\vec{E}^s = \mathbf{F} \cdot \vec{E}^i = \mathbf{F} \cdot \sum_{q_i} \hat{q}_i \hat{q}_i \cdot \vec{E}_l^i.$$

And also

$$\vec{E}^s = \sum_{p_s} \hat{p}_s \hat{p}_s \cdot \vec{E}_l^s = \sum_{p_s} \hat{p}_s \hat{p}_s \cdot \mathbf{F}' \cdot \vec{E}_l^i$$

$$= \mathbf{F} \cdot \sum_{q_i} \hat{q}_i \hat{q}_i \cdot \vec{E}_l^i.$$

Simplifying the last two terms

$$\sum_{p_s} \hat{p}_s \hat{p}_s \cdot \mathbf{F}' = \mathbf{F} \cdot \sum_{q_i} \hat{q}_i \hat{q}_i$$

and multiplying by \hat{p}_s on the right and \hat{q}_i on the left

$$\hat{p}_s \cdot \sum_{p_s} \hat{p}_s \hat{p}_s \cdot \mathbf{F}' \cdot \hat{q}_i = \hat{p}_s \cdot \mathbf{F} \cdot \sum_{q_i} \hat{q}_i \hat{q}_i \cdot \hat{q}_i$$

$$\hat{p}_s \cdot \mathbf{F}' \cdot \hat{q}_i = \hat{p}_s \cdot \mathbf{F} \cdot \hat{q}_i = F_{pq}$$

$$F_{pq} = \hat{p}_s \cdot \sum_{p_{sl}} \sum_{q_{il}} F'_{pq}(\hat{p}_{sl} \hat{q}_{il}) \cdot \hat{q}_i$$

$$= \sum_{p_{sl}} \sum_{q_{il}} F'_{pq}(\hat{p}_s \cdot \hat{p}_{sl})(\hat{q}_{il} \cdot \hat{q}_i).$$

REFERENCES

- [1] S. T. Lowe, J. L. LaBrecque, C. Zuffada, L. J. Romans, L. E. Young, and G. A. Hajj, "First spaceborne observation of an earth-reflected GPS signal," *Radio Sci.*, vol. 37, no. 1, pp. 1–28, 2002.
- [2] M. Martin-Neira, M. Caparrini, J. Font-Rossello, S. Lannelongue, and C. Serra Vallmitjana, "The PARIS concept: An experimental demonstration of sea surface altimetry using GPS reflected signals," *IEEE Trans. Geosci. Remote Sens.*, vol. 39, no. 1, pp. 142–150, Jan. 2001.
- [3] N. Sánchez *et al.*, "On the synergy of airborne GNSS-R and landsat 8 for soil moisture estimation," *Remote Sens.*, vol. 7, no. 8, pp. 9954–9974, 2015.
- [4] S. V. Nghiem *et al.*, "Wetland monitoring with global navigation satellite system reflectometry," *Earth Space Sci.*, vol. 4, no. 1, pp. 16–39, 2017.
- [5] A. Egido *et al.*, "Global navigation satellite systems reflectometry as a remote sensing tool for agriculture," *Remote Sens.*, vol. 4, no. 8, pp. 2356–2372, 2012.

- [6] A. Egido *et al.*, "Airborne GNSS-R polarimetric measurements for soil moisture and above-ground biomass estimation," *IEEE J. Sel. Topics Appl. Earth Observ. Remote Sens.*, vol. 7, no. 5, pp. 1522–1532, May 2014.
- [7] C. Chew, R. Shah, C. Zuffada, G. Hajj, D. Masters, and A. Mannucci, "Demonstrating soil moisture remote sensing with observations from the UK TechDemoSat-1 satellite mission," *Geophys. Res. Lett.*, vol. 43, no. 7, pp. 3317–3324, 2016.
- [8] A. Camps *et al.*, "Sensitivity of GNSS-R spaceborne observations to soil moisture and vegetation," *IEEE J. Sel. Topics Appl. Earth Observ. Remote Sens.*, vol. 9, no. 10, pp. 4730–4742, Oct. 2016.
- [9] V. U. Zavorotny and A. G. Voronovich, "Scattering of GPS signals from the ocean with wind remote sensing application," *IEEE Trans. Geosci. Remote Sens.*, vol. 38, no. 2, pp. 951–964, Mar. 2000.
- [10] A. G. Voronovich and V. U. Zavorotny, "Bistatic radar equation for signals of opportunity revisited," *IEEE Trans. Geosci. Remote Sens.*, vol. 56, no. 4, pp. 1959–1968, Apr. 2018.
- [11] H. Park *et al.*, "A generic level 1 simulator for spaceborne GNSS-R missions and application to GEROS-ISS ocean reflectometry," *IEEE J. Sel. Topics Appl. Earth Observ. Remote Sens.*, vol. 10, no. 10, pp. 4645–4659, Oct. 2017.
- [12] H. Park, A. Camps, D. Pascual, A. Alonso-Arroyo, J. Querol, and R. Onrubia, "Improvement of PAU/PARIS end-to-end performance simulator (P2EPS): Land scattering including topography," in *Proc. IEEE Int. Geosci. Remote Sens. Symp.*, 2016, pp. 5607–5610.
- [13] F. Fabra, E. Cardellach, W. Li, and A. Rius, "WAVPY: A GNSS-R open source software library for data analysis and simulation," in *Proc. IEEE Int. Geosci. Remote Sens. Symp.*, 2017, pp. 4125–4128.
- [14] X. Wu and S. Jin, "GNSS-reflectometry: Forest canopies polarization scattering properties and modeling," *Adv. Space Res.*, vol. 54, no. 5, pp. 863–870, 2014.
- [15] P. Liang, L. E. Pierce, and M. Moghaddam, "Radiative transfer model for microwave bistatic scattering from forest canopies," *IEEE Trans. Geosci. Remote Sens.*, vol. 43, no. 11, pp. 2470–2483, Nov. 2005.
- [16] O. Eroglu, M. Kurum, and J. Ball, "Response of GNSS-R on dynamic vegetated terrain conditions," *IEEE J. Sel. Topics Appl. Earth Observ. Remote Sens.*, vol. 12, no. 5, pp. 1599–1611, May 2019.
- [17] M. Kurum, M. Deshpande, A. T. Joseph, P. E. O'Neill, R. H. Lang, and O. Eroglu, "SCoBi-Veg: A generalized bistatic scattering model of reflectometry from vegetation for signals of opportunity applications," *IEEE Trans. Geosci. Remote Sens.*, vol. 57, no. 2, pp. 1049–1068, Feb. 2019.
- [18] W. Gu, H. Xu, and L. Tsang, "A numerical kirchhoff simulator for GNSS-R land applications," *Prog. Electromagn. Res.*, vol. 164, pp. 119–133, 2019.
- [19] J. Zhu, L. Tsang, and H. Xu, "A physical patch model for GNSS-R land applications," *Prog. Electromagn. Res.*, vol. 165, pp. 93–105, 2019.
- [20] N. Pierdicca, L. Guerriero, R. Giusto, M. Brogioni, and A. Egido, "SAVERS: A simulator of GNSS reflections from bare and vegetated soils," *IEEE Trans. Geosci. Remote Sens.*, vol. 52, no. 10, pp. 6542–6554, Oct. 2014.
- [21] H. Carreno-Luengo, G. Luzi, and M. Crosetto, "First evaluation of topography on GNSS-R: An empirical study based on a digital elevation model," *Remote Sens.*, vol. 11, no. 21, 2019, Art. no. 2556.
- [22] D. Comite, F. Ticconi, L. Dente, L. Guerriero, and N. Pierdicca, "Bistatic coherent scattering from rough soils with application to GNSS reflectometry," *IEEE Trans. Geosci. Remote Sens.*, vol. 58, no. 1, pp. 612–625, Jan. 2020.
- [23] A. Camps, "Spatial resolution in GNSS-R under coherent scattering," *IEEE Geosci. Remote Sens. Lett.*, vol. 17, no. 1, pp. 32–36, Jan. 2020.
- [24] P. Ferrazzoli, L. Guerriero, N. Pierdicca, and R. Rahmoune, "Forest biomass monitoring with GNSS-R: Theoretical simulations," *Adv. Space Res.*, vol. 47, no. 10, pp. 1823–1832, 2011.
- [25] T. D. Wu and K. S. Chen, "A reappraisal of the validity of the IEM model for backscattering from rough surfaces," *IEEE Trans. Geosci. Remote Sens.*, vol. 42, no. 4, pp. 743–753, Apr. 2004.
- [26] A. K. Fung and H. J. Eom, "Coherent scattering of a spherical wave from an irregular surface," *IEEE Trans. Antennas Propag.*, vol. 31, no. 1, pp. 68–72, Jan. 1983.
- [27] M. Bracaglia, P. Ferrazzoli, and L. Guerriero, "A fully polarimetric multiple scattering model for crops," *Remote Sens. Environ.*, vol. 54, pp. 170–179, 1995.
- [28] M. A. Karam and A. K. Fung, "Electromagnetic scattering from a layer of finite length, randomly oriented, dielectric, circular cylinders over a rough interface with application to vegetation," *Int. J. Remote Sens.*, vol. 9, pp. 1109–1134, 1988.
- [29] M. Brogioni *et al.*, "Sensitivity of bistatic scattering to soil moisture and surface roughness of bare soils," *Int. J. Remote Sens.*, vol. 31, no. 15, pp. 4227–4255, 2010.
- [30] M. C. Dobson, F. T. Ulaby, M. T. Hallikainen, and M. A. El-Rayes, "Microwave dielectric behavior of wet soil—Part II: Dielectric mixing models," *IEEE Trans. Geosci. Remote Sens.*, vol. GE-23, no. 1, pp. 35–46, Jan. 1985.
- [31] L. Guerriero, N. Pierdicca, L. Pulvirenti, and P. Ferrazzoli, "Use of satellite radar bistatic measurements for crop monitoring: A simulation study on corn fields," *Remote Sens.*, vol. 5, no. 2, pp. 864–890, 2013.
- [32] H. J. Eom and A. K. Fung, "A scatter model for vegetation up to Ku-band," *Remote Sens. Environ.*, vol. 15, no. 3, pp. 185–200, 1984.
- [33] L. Guerriero *et al.*, "Ground-based remote sensing of forests exploiting GNSS signals," *IEEE Trans. Geosci. Remote Sens.*, to be published, doi: 10.1109/TGRS.2020.2976899
- [34] M. S. Burgin, U. K. Khankhoje, X. Duan, and M. Moghaddam, "Generalized terrain topography in radar scattering models," *IEEE Trans. Geosci. Remote Sens.*, vol. 54, no. 7, pp. 3944–3952, Jul. 2016.
- [35] M. Unwin, P. Jales, J. Tye, C. Gommenginger, G. Foti, and J. Rosello, "Spaceborne GNSS-reflectometry on techdemosat-1: Early mission operations and exploitation," *IEEE J. Sel. Topics Appl. Earth Observ. Remote Sens.*, vol. 9, no. 10, pp. 4525–4539, Oct. 2016.
- [36] N. Pierdicca *et al.*, "Spaceborne GNSS reflectometry data for land applications: An analysis of techdemosat data," in *Proc. Int. Geosci. Remote Sens. Symp.*, 2018, pp. 3343–3346.
- [37] T. Wang, C. S. Ruf, B. Block, D. S. McKague, and S. Gleason, "Design and performance of a GPS constellation power monitor system for improved CYGNSS L1B calibration," *IEEE J. Sel. Topics Appl. Earth Observ. Remote Sens.*, vol. 12, no. 1, pp. 26–36, Jan. 2019.
- [38] M. Simard, N. Pinto, J. B. Fisher, and A. Baccini, "Mapping forest canopy height globally with spaceborne lidar," *J. Geophys. Res.*, vol. 116, 2011, Art. no. G04021.
- [39] E. Loria *et al.*, "Analysis of wetland extent retrieval accuracy using CYGNSS," in *Proc. IEEE Int. Geosci. Remote Sens. Symp.*, 2019, pp. 8684–8687.
- [40] J. C. Jenkins, D. C. Chojnacky, L. S. Heath, and R. A. Birdsey, "National-scale biomass estimators for United States tree species," *Forest Sci.*, vol. 49, no. 1, pp. 12–35, 2003.
- [41] A. Della Vecchia *et al.*, "Modeling the multifrequency emission of broadleaf forests and their components," *IEEE Trans. Geosci. Remote Sens.*, vol. 48, no. 1, pp. 270–272, Jan. 2010.
- [42] V. Avitabile, M. Herold, S. L. L. Heuvelink, O. L. Phillips, and G. P. Asner, "An integrated pan-tropical biomass maps using multiple reference datasets," *Global Change Biol.*, vol. 22, no. 4, pp. 1406–1420, 2016.
- [43] A. Camps, M. Vall-Lloera, H. Park, G. Portal, and L. Rossato, "Sensitivity of TDS-1 GNSS-R reflectivity to soil moisture: Global and regional differences and impact of different spatial scales," *Remote Sens.*, vol. 10, 2018, Art. no. 1856.
- [44] M. C. Dobson, F. T. Ulaby, T. LeToan, A. Beaudoin, E. S. Kasischke, and N. Christensen, "Dependence of radar backscatter on coniferous forest biomass," *IEEE Trans. Geosci. Remote Sens.*, vol. 30, no. 2, pp. 412–415, Mar. 1992.
- [45] M. Zribi *et al.*, "Performance of GNSS-R GLORI data for biomass estimation over the land forest," *Int. J. Appl. Earth Observ. Geoinf.*, vol. 74, pp. 150–158, 2019.



Laura Dente received the Laurea degree in physics from the University of Bari, Bari, Italy, in 2000, and the Ph.D. degree from the University of Twente, Enschede, The Netherlands, in 2016.

In 2002, she worked as Young Graduate Trainee with ESA-ESTEC, The Netherlands, and from 2003 to 2006 as Research Fellow at CNR-ISSIA, Italy, on soil moisture and biomass retrieval from SAR data. From 2007 to 2012, she was a Trainee Research Assistant with the University of Twente (ITC Faculty) focusing on passive and active microwave remote sensing for soil moisture monitoring. Since 2016, she has been a Research Fellow with the University of Rome Tor Vergata, Roma RM, Italy, where her main research interests include GNSS reflectometry and its application over land.



Leila Guerriero (Member, IEEE) received the Laurea degree in physics from Sapienza University of Rome, Rome, Italy, in 1986, and the Ph.D. degree in electromagnetism from the University of Rome Tor Vergata, Roma RM, Italy, in 1991.

Since 1994, she has been a Permanent Researcher with Tor Vergata University, Roma RM, Italy, where she is currently an Associate Professor holding the courses on earth satellite observation and on geoinformation. Her activities are mainly concerned with modeling microwave scattering and emissivity from agricultural and forested areas. She participated to several international projects, among them: in 1988, she was involved in a cooperation between JPL and Italian National Research Council for investigations on geophysical applications of Imaging Spectrometry in InfraRed and Visible Remote Sensing. In 1995, she participated to the ESA project on Radiometric Polarimetry of ocean surfaces. In 1999–2001, she participated at the EEC concerted action ERA-ORA whose objective was to improve radar data analysis and utilization. More recently, she has been part of the teams of the ESA projects “Soil Moisture and Ocean Salinity Satellite,” “Development of SAR inversion algorithms for land applications,” “Use of Bistatic Microwave Measurements for Earth Observation,” “SAOCOM-CS bistatic imaging, radiometry, and interferometry over land.” Lately, she has been involved in the modeling of GNSS-R signals in the FP7 “EGEM - European GNSSR Environmental Monitoring,” in the H2020 “COREGAL – Combined Positioning Reflectometry Galileo Code Receiver for Forest Management” (both within the European Union Framework Program) and in the ESA projects “LEIMON: Land monitoring with navigation signals,” “GRASS: GNSS-Reflectometry Analysis for Biomass Monitoring,” and “Spaceborne GNSS-R for Land Applications.”

Dr. Guerriero is a member of the Permanent Steering Scientific Committee of MicroRad.



Nazzareno Pierdicca (Senior Member, IEEE) received the Laurea degree in electronic engineering (*cum laude*) from the University “La Sapienza” of Rome, Rome, Italy, in 1981.

From 1978 to 1982, he worked with the Italian Agency for Alternative Energy. From 1982 to 1990, he was working with Telespazio, Rome, Italy, in the Remote Sensing Division. In November 1990, he joined the Department of Information Engineering, Electronics and Telecommunications, Sapienza University of Rome. He is currently a Full Professor and teaches remote sensing, antenna, and electromagnetic fields with the Faculty of Engineering, Sapienza University of Rome. His research interests include electromagnetic scattering and emission models for sea and bare soil surfaces and their inversion, microwave radiometry of the atmosphere, and radar land applications.

Prof. Pierdicca is a Past Chairman of the GRSS Central Italy Chapter.



Davide Comite (Member, IEEE) received the master's (*cum laude*) degree in telecommunications engineering and the Ph.D. degree in electromagnetics and mathematical models for engineering from “Sapienza” University, Rome, Italy, in 2011 and 2015, respectively.

He is currently a Postdoctoral Researcher with Sapienza University. He was a Visiting Ph.D. Student with the Institute of Electronics and Telecommunications of Rennes, University of Rennes 1, France, from March to June 2014, and a Postdoctoral Researcher at

the Center of Advanced Communications, Villanova University, PA, USA, from April to December 2015. His scientific research interests include the study of the scattering from natural surfaces as well as the GNSS reflectometry over the land, the microwave imaging and objects detection performed through GPR, and the modeling of the radar signature in forward scatter radar systems. He is also interested in the study and design of leaky-wave antennas and the generation of nondiffracting waves and pulses.

Dr. Comite has been the recipient of a number of awards at national and international conferences. He received the *Publons Top Peer Reviewers Award* for both *Geoscience and Engineering* in September 2018, and for *Cross-fields* in 2019. In 2019, the IEEE Antennas and Propagation Society recognized him as an Outstanding Reviewer for the IEEE TRANSACTIONS ON ANTENNAS AND PROPAGATION. He currently serves as a reviewer for several international journals. He is an Associate Editor of the *IET Journal of Engineering*, *IET Microwaves, Antennas and Propagation* by the Institution of Engineering and Technology, and IEEE ACCESS. He is an URSI Senior Member.